Simulation of Heat and Mass Transfer in a Grain Pile on the Basis of a 2D Irregular Pore Network

Pengxiao Chen[1], Kai Huang[1, 2], Fenghe Wang[1], Weijun Xie[1], Shuo Wei[1] and Deyong Yang[1, *]

Abstract: The so-called pore network model has great advantages in describing the process of heat and mass transfer in porous media. In order to construct a random two-dimensional (2D) irregular pore network model for an unconsolidated material, image processing technology was used to extract the required topological and geometric information from a 2D sample of soybean particles, and a dedicated algorithm was elaborated to merge some adjacent small pores. Based on the extracted information, a 2D pore network model including particle information was reconstructed and verified to reflect the pore structure of discrete particles. This method was used to reconstruct a random 2D irregular pore network model of wheat. Accordingly, a multi-scale heat and mass transfer model was implemented to simulate the drying of wheat. The simulation results were consistent with the experimental results, which indicates that the reconstructed irregular pore network model can effectively simulate the real pore structure inside unconsolidated porous media. The present approach may be regarded as the foundation for establishing in the future a three-dimensional pore network model and studying the heat and mass transfer process in a grain pile.

Keywords: MATLAB, pore network, heat and mass transfer, thiessen polygon.

Nomenclature

W_t	width of the throat
S	rectangular area
S_1	total area of particles in 2D image
S_P	total area of pores
L_t	total length of throats
y	the number of throats at a certain length
l	length of a throat, m
ε	porosity

---

[1] College of Engineering, China Agricultural University, Beijing, China.

[2] College of Engineering, Nanjing Agricultural University, Nanjing, China.

[*] Corresponding Author: Deyong Yang. Email: ydy@cau.edu.cn.

ρ	wet air density, kg/m³
k^*	permeability, m²
μ	wet air viscosity, Pa·s
∇	laplacian operator
P	wet air pressure, Pa
r_t	throat radius, m
num_{i1}	total number of pores connected to the pore i_1
V_d	volume of a pore, m³
ρ_v	vapor density within pore, kg/m³
v_t	air speed in throat, m/s
A_g	surface area of particle, m²
G	phenomenological coefficient
R	particle radius, m
Δr	the thickness of the single layer after dividing the particle into m_t layers along the radius
j	jth calculation on the particle scale
$\Delta \tau$	the interval between each calculation time, $\Delta t = 10\Delta \tau$
K	convective mass transfer coefficient, m/s
ρ_{veq}	vapor density at particle surface, kg/m³
num_{i3}	total number of particle around the pore i_3
k_1	number of pores around a particle
e	sign of wind flowing into a pore
o	sign of wind out of a pore
T	air temperature in a pore, K
C	specific heat capacity of air, kJ/(kg·K)
ρ	air density, kg/m³
h	convective heat transfer coefficient, W/(m²·K)
T_g	particle temperature, K
D	mass diffusion coefficient, m²/s
r	spherical coordinates
M	dry-basis moisture content of particle
M_e	dry-basis equilibrium moisture content of particle
h_{fg}	latent heat of water, kJ/kg
C_v	specific heat capacity of vapor, kJ/(kg·K)
W	mass of evaporated water from grain particle in unit time, kg/s
C_w	specific heat capacity of water, kJ/(kg·K)
	specific heat capacity of dry grain particle, kJ/(kg·K)

C_g

ρ_g density of dry grain particle, kg/m^3

1 Introduction

Traditionally, many heat and mass transfer studies of porous media are based on the assumption of continuous media, which treat materials as isotropic. On this basis, partial differential equations are established for heat and mass transfer simulation [Abbouda and Al-Amri (2001); Jia, Sun and Cao (2001); Ali, Al and Sirelkhatim (2004); Hammami, Ben and Mami (2016)]. However, this method relies on the semi-empirical model and cannot reveal the influence of the microstructure characteristics of the material on the transmission process. In contrast, the pore network method, which is mainly applied in the research fields of petroleum, geology, soil, plant tissues, and fuel cells, etc., can reveal the topological relationship and geometric information of the pore space in the porous medium. Combined with the corresponding discrete mathematical equations, it can be used to simulate the heat and mass transfer process inside porous media. Therefore, it is of great significance to apply the pore network model to the field of heat and mass transfer simulation of porous media.

At present, there are three types of pore network models, including the conceptual model [Xie, Wang, Wang et al. (2016)], statistical model [Banerjee, Bevilacqua, Eifert et al. (2019); Gharedaghloo, Price, Rezanezhad et al. (2018); Salama (2018)] and image reconstruction model [Ma, Sanchez, Wu et al. (2014); Wang, Zhao, Zhang et al. (2016)]. The conceptual pore network model consists of pores and throats based on some assumptions, which is primarily used to explain the physical or chemical characteristics of porous media qualitatively or semiquantitatively. Erickson et al. [Erickson, Li and Park (2002)] found that the nonuniform capillary has a significant lower wetting ability than the uniform capillary, and any change in the uniform capillary diameter will reduce the overall wetting rate inevitably. Young [Young (2004)] obtained the same result by constructing a simple formula to simulate the wicking flow in a nonuniform capillary. On the basis of Darcy's Law and mass conservation, Liu et al. [Liu, Wu, Gan et al. (2018)] developed a theoretical model of capillary penetration combining evaporation effects in 2D homogeneous porous media of varying cross-sections, which was further examined by numerical simulations. The effects of sample geometry and liquid evaporation on capillary penetration are quantitatively analyzed.

The statistical pore network model is constructed based on the extracted statistical structural parameters of pores and throats from the real pore network [Yao, Zhao and Yi (2005); Oren and Bakke (2002); Yu, Duan Chen et al. (2018)]. The model has good similarity to the real pore space and can explain the physical and chemical characteristics of porous media. However, some different pore network models exist obeying the same statistical law, which means the statistical model has multiple solutions. Fatt [Fatt (1956)] constructed a pore network model based on the 2D model of the circuit network and achieved a good prediction of the macroscopic properties of rock. However, the proposed model can only calculate some parameters, such as the distribution of the pore and throat. For porous media reconstruction, Lu and Torquato et al. [Lu and Torquato (1992)] used the linear path function as a statistical function and improved the overall characteristics

of porous media. In the early 1990s, Daian and Saliba introduced the pore network method into the research field of porous media drying [Daian and Saliba (1991)]. In the study of the drying process of rigid porous media, Prat [Prat (1993)] combined seepage theory with pore network theory and obtained the phase distribution and drying rate curve at different times during the drying of porous media. The combination of pore network theory and drying theory has promoted the application of pore network theory in simulating the drying process [Laurindo and Prat (1998); Laurindo and Prat (1996); Prat (1995); Segura and Toledo (2005)]. In 2006, Yang [Yang (2006)] established a mathematical drying model based on a 2D fractal pore network, and the simulated drying curve of a potato slice was more consistent with the experimental results than the drying model based on the regular pore network. Gong et al. [Gong, Niu, Dong et al. (2009)] obtained the microstructure parameters of the frozen-dried potato through a mercury intrusion experiment, and the fractal dimension of pores by calculation.

The image reconstruction pore network model is completely based on the scanned three-dimensional images or the combination of a series two-dimensional images. The specific locations of pores and throats should be determined during reconstruction. Therefore, it is the closest to the real pore structure. It is suitable for developing a small pore network model limited by the image size. Based on actual solid particle accumulation, Wang et al. [Wang, Kharaghani, Metzger et al. (2012)] obtained a three-dimensional X-ray scanned image, extracted the pore network information, and simulated the liquid transfer and drying processes in pores. The simulation results were largely consistent with the experimental results. However, the pore network information comes from the actual stacking material and cannot be used to reconstruct a pore network model with a random size. To solve this problem, Zhao et al. [Zhao, Liu, Han et al. (2018)] developed a three-dimensional reconstruction technique based on the marching cubes algorithm and ray casting algorithm, which restored the geometry and spatial distribution of soil pores. The ray casting algorithm can clearly reflect the pore contour and the detailed pore structure information compared with the marching cubes algorithm.

Most of the processes of heat and mass transfer only occurred in pore space but not between the skeleton and pore space in the above studies, which is not in line with the actual situation, especially in the hygroscopic porous media. Therefore, it is necessary to combine the particle information with the pore and throat information in the porous medium. Yuan et al. [Yuan, Tan, Zhao et al. (2016)] constructed a regular pore network of unconsolidated corn kernels by statistical methods and established the multiscale heat and mass transfer models for simulating the drying process of corn. Yue et al. [Yue and Zhang (2017)] developed an algorithm to construct a tetrahedral model, equivalently obtained the pore space and pore structures in bulk grain, and then calculated the airflow distribution in the pore space. Kharaghani et al. [Kharaghani, Metzger and Tsotsas (2012)] constructed an irregular pore network model for convective drying of random aggregates composed of mono-sized primary particles, and an isothermal pore network drying model based on invasion percolation driven by evaporation. The simulation results are in line with the actual drying conditions. However, the moisture is dried only in pore space and does not exchange with the skeleton. There are some shorter throats in the pore network model, which are not merged and inconsistent with the actual structure.

In this study, soybean was selected as the test material for extracting pore space information and particle information from a 2D unconsolidated porous medium by MATLAB image processing technology. Based on Thiessen polygons, an irregular 2D pore network model reflecting the real accumulation structure of the grain pile was constructed, which can be seen as a pore network structure used to simulate any nonconsolidated porous media stacked structure. Combined the constructed irregular pore network model, a heat and mass transfer model was established to simulate the drying process of particulate material and verified by a wheat drying experiment. It is helpful for constructing a 2D and 3D irregular pore network of unconsolidated material, simulating the heat and mass transfer process in porous media.

2 Construction of a 2D irregular pore network

2.1 Extraction of structural parameters from an 2D image

Most agricultural materials are irregular and the size of an irregularly shaped object can be described by the tri-axial dimensions-length (L), width (W) and thickness (T). It is difficult to address irregular particles, so an irregular particle is often taken as a sphere, and the equivalent radius Rp can be calculated by Eq. (1).

$$R_p = \frac{\sqrt[3]{LWT}}{2} \tag{1}$$

Monolayer soybeans were randomly placed in a 0.1 m×0.1 m area until soybeans filled the entire rectangular space. The scanned 2D image of monolayer soybeans was processed by MATLAB software. Through binary image processing Fig. 1(b), particle skeleton segmentation Fig. 1(c), and watershed segmentation Fig. 1(d), the particle information and the topological structure of the pore space in the 2D image were obtained.

The particle number, position and area can be determined by particle skeleton segmentation and the connected region tag function, and the center and equivalent diameter of an equivalent circle with the same area of the particle can be obtained.

The intersections in Fig. 1(d) are considered as the centers of pores, and the edges are considered as the centerline between two adjacent pores.

During watershed segmentation, some short edges can appear, as shown in Fig. 2(a). The vertices A1 and A2 represent the centers of two adjacent pores, but the two small pores should belong to the same larger pore. Therefore, it is necessary to identify this situation and merge the small pores to obtain the pore parameters that are closer to the actual pore structure. The midpoint A3 of A1, A2 is the new center of the merged pore, as shown in Fig. 2(b).
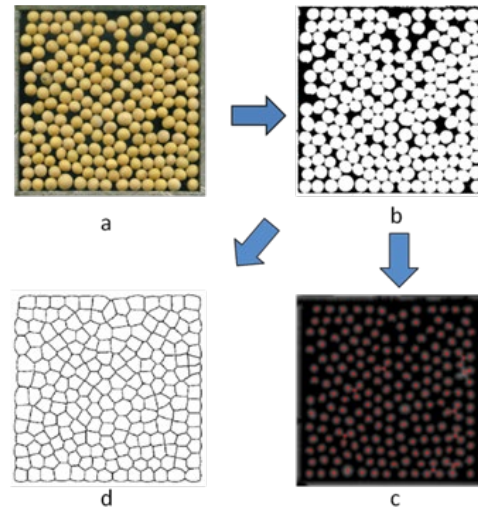
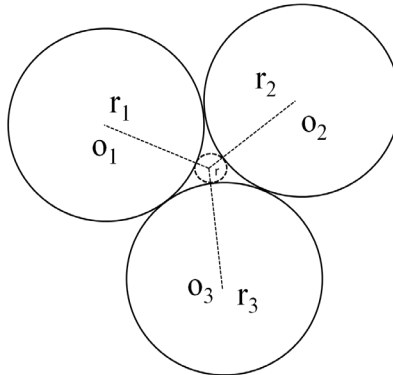**Figure 1:** Schematic diagram of extracting pore network information
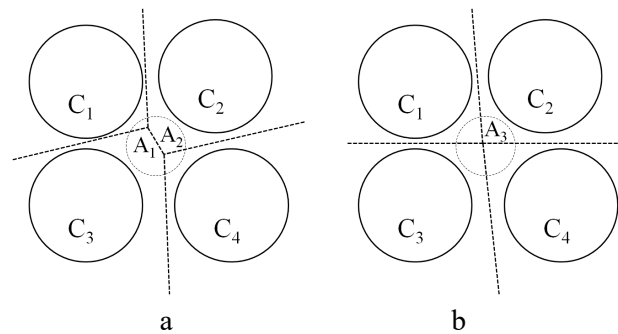
Figure 2: Schematic diagram of pores merging

The minimum pore appears when the three circles surrounding the pore are tangent to each other, as shown in Fig. 3, and the minimum coordination number is 3. The minimum pore radius r can be obtained by Eq. (2) [Xudong (2005)].

$$r = \frac{r_1 r_2 r_3}{r_1 r_2 + r_1 r_3 + r_2 r_3 + 2\sqrt{r_1 r_2 r_3 (r_1 + r_2 + r_3)}} \tag{2}$$

where r1, r2, r3 are the radii of the three circumscribed circles. Since soybean particles are taken as equal-diameter spheres, then r1=r2=r3=R. R is the extracted average equivalent radius of soybeans. Eq. (2) is transformed into Eq. (3).

$$r = \frac{R}{3 + 2\sqrt{3}} \tag{3}$$

**Figure 3:** Schematic diagram of a minimum pore

Therefore, the edges smaller than 2r cannot reflect the actual throat condition, and the small pores should be merged and a new center can be obtained.

The pore radius can be extracted based on the maximum sphere algorithm, and the throat length can be calculated though the centerline spacing and the radii of two adjacent pores. Assuming the width of all throats is consistent, and the throat width can be calculated by Eq. (4). The coordination number is equal to the number of edges connected to a pore.

$$W_t = \frac{S - S_1 - S_p}{L_t} \tag{4}$$

According to the above processing, 193 particles, 382 pores, and 573 throats were obtained from Fig. 1. The average coordination number is 3.00. The equivalent radius distributions of soybean particles and extracted particles from the image are shown in Fig. 4. The average equivalent radius of extracted particles is 3.4443 mm, which is consistent with the average equivalent radius of soybean particles of 3.4496 mm.
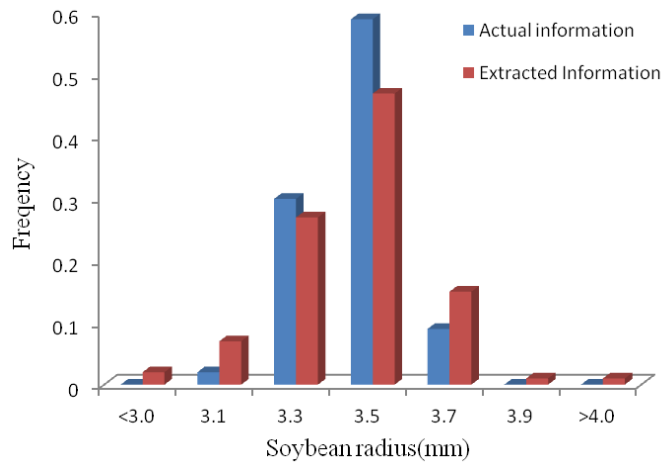
Figure 4: Equivalent radius distribution of soybeans

The extracted parameter distribution of the coordination number, the throat length and the pore radius are shown in Figs. 7-9 respectively. The throat length mainly distributed

between 3 mm and 7 mm with the normal distribution. After fitting, the throat length distribution roughly conforms to formula (5):

$$y = \frac{1}{1.07\sqrt{2\pi}} e^{-\frac{(l-3)^2}{2.2896}} \quad (l = 2,3,4,5,6) \tag{5}$$

The pore radius generally varies between 0.7 mm and 1.5 mm, as shown in Fig. 8, which is smaller than the radius of soybeans. There are also some large pores caused by friction, as the soybean surface is not completely smooth and the shape is not completely spherical. The calculated porosity from the image is 27.85%, and the throat width is 0.2761 mm according to Eq. (4). The extracted porosity is smaller than the real porosity of the grain pile because the pore space in the 2D image is just the minimum projection area of the real pore space on the normal projection plane. Therefore, the 2D pore network model is limited in simulating the three-dimensional pore space.
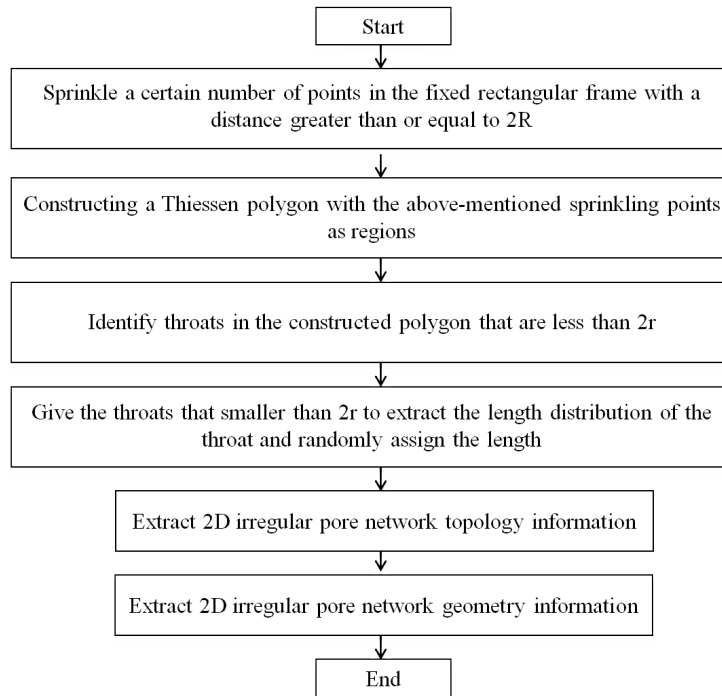
2.2 Construction of a 2D irregular pore network model based on the extracted parameters

By analyzing the extracted parameters and considering the narrow distribution of the equivalent diameter and the effect of image noise on the extracted parameters, it follows that soybean particles can be regarded as equal-diameter spheres with a radius of 3.44 mm. According to the principle of Thiessen polygons, this paper argues that this construction can accurately describe the 2D soybean accumulation.

OpenGL technology is used to sprinkle a certain number of equal-diameter circles randomly inside the fixed rectangular area. Moreover, all of the equal-diameter circles do not intersect each other. Therefore, the position of each circle center can be obtained, and the central distance between two adjacent circles is greater than or equal to the diameter 2R of the circle. Based on above circle centers, Thiessen polygons are constructed, and the topological information and geometric information are obtained following the similar process of extraction.

A new value is identified and reassigned to the short edges with the length less than 2r according to Eq. (3), and the topology information and geometric information of the 2D irregular pore network model are updated. The flow chart of the construction program is shown in Fig. 5.

```
┌─────────────┐
│    Start    │
└─────────────┘
       ↓
┌──────────────────────────────────────────────────────────────┐
│ Sprinkle a certain number of points in the fixed rectangular  │
│      frame with a distance greater than or equal to 2R        │
└──────────────────────────────────────────────────────────────┘
       ↓
┌──────────────────────────────────────────────────────────────┐
│ Constructing a Thiessen polygon with the above-mentioned      │
│              sprinkling points as regions                     │
└──────────────────────────────────────────────────────────────┘
       ↓
┌──────────────────────────────────────────────────────────────┐
│ Identify throats in the constructed polygon that are less     │
│                        than 2r                                │
└──────────────────────────────────────────────────────────────┘
       ↓
┌──────────────────────────────────────────────────────────────┐
│ Give the throats that smaller than 2r to extract the length   │
│   distribution of the throat and randomly assign the length   │
└──────────────────────────────────────────────────────────────┘
       ↓
┌──────────────────────────────────────────────────────────────┐
│    Extract 2D irregular pore network topology information     │
└──────────────────────────────────────────────────────────────┘
       ↓
┌──────────────────────────────────────────────────────────────┐
│    Extract 2D irregular pore network geometry information     │
└──────────────────────────────────────────────────────────────┘
       ↓
┌─────────────┐
│     End     │
└─────────────┘
```

Figure 5: Flow chart of constructing a pore network model

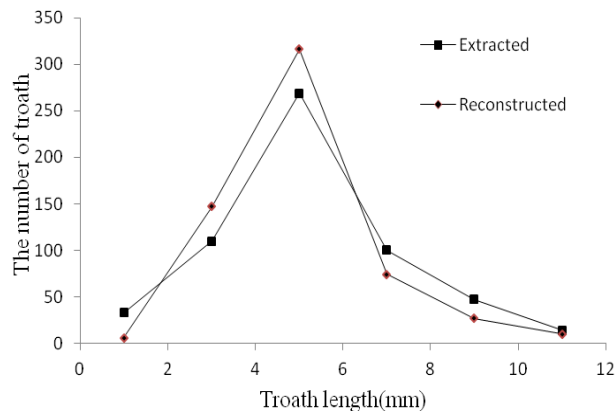Fig. 6 shows the constructed 2D irregular pore network model in a 0.1 m×0.1 m area. The vertex and edge of a polygon represent the pore and throat, respectively, and the closed space in the polygon represents the particle region. Comparing the extracted parameters from a 2D image and the parameters in the reconstructed 2D irregular pore network, all the parameter distributions are very similar, as shown in Figs. 6-8. The reconstructed coordination number and the throat length are consistent with the extracted parameters, and some large pores appear in the reconstructed pore network model caused by the uneven distribution near the rectangular edge during the reconstruction process. The differences between the extracted parameters and the reconstructed parameters are shown in Tab. 1.
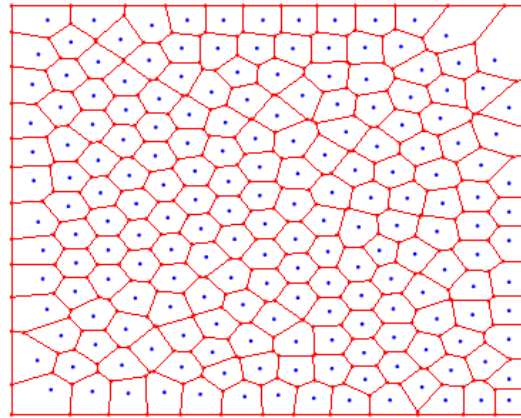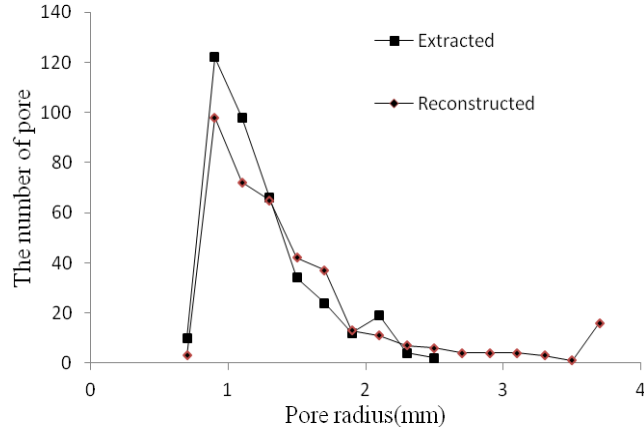
Figure 6: 2D irregular pore network of soybean
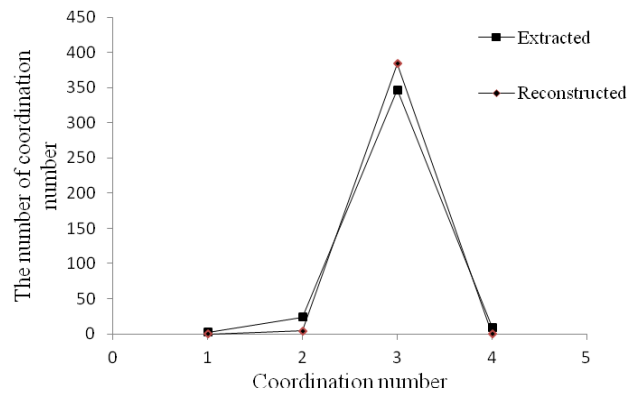
Figure 7: Coordination number of pores in a 2D irregular pore network

Figure 8: Throat length in a 2D irregular pore network

Figure 9: Pore radius in a 2D irregular pore network

Table 1: Differences between the extracted parameters and the reconstructed parameters

Parameter	Extracted	Reconstructed
Particle number	193	193
Pore number	382	388
Throat number	573	580
Porosity (%)	27.85	28.25
Throat width (mm)	0.2761	0.2661
Average coordination number	3.00	2.99

There are 193 particle regions, 388 pores and 580 throats in the reconstructed 2D irregular pore network model. In addition, the porosity of the pore network model is 28.25%. The throat width is 0.2661 mm, which is slightly larger than the extracted parameters. The average coordination number is 2.99, which is slightly smaller than the extracted parameters. The maximum error of the throat width is 3.62%, and the minimum error of the average coordination number is 0.33%, while the errors of other parameters are less than 2%. Therefore, the reconstructed model can well reflect the pore structure of granular materials and can be used to construct a large-scale pore network model.

The previous 2D pore network models based on a slice were mostly regular pore network models. The particle radius, pore radius and throat length are assigned according to their distributions and a certain rule, which is considered equivalent to an irregular pore network model. However, the particle radius distribution obtained from a slice is very different from the real particle radius distribution, and the coordination number of a regular pore network model is fixed, which is 4 in a frequently used regular rectangular pore network model except for the boundary. It cannot match the particle size and the actual pore network parameters in bulk grain. The method of constructing a 2D pore network model in this paper is different from the previous method, and it can reflect the real particle size and the pore network parameters in a 2D image.

2.3 Construction of a 2D irregular pore network model of wheat

A wheat kernel is approximately ellipsoid; its equivalent radius of more than 93.5% of wheat particles is relatively concentrated at 1.90~2.20 mm in this study, as shown in Fig. 10. Although there is a certain deviation between the shape of a wheat kernel and a sphere, wheat particles are taken as equal-diameter spheres with an equivalent radius of 2 mm to construct the pore network model.

Based on the above method and the equivalent size of a wheat kernel, a 2D irregular pore network model of wheat is constructed in a 0.1 m×0.1 m container, as shown in Fig. 11. Therefore, 631 wheat kernels, 1264 pores and 1894 throats are obtained, and the average coordination number is 2.997.
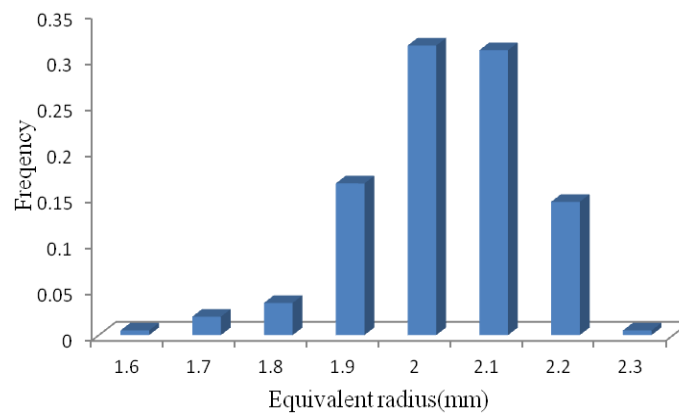
Figure 10: Equivalent radius of wheat kernels
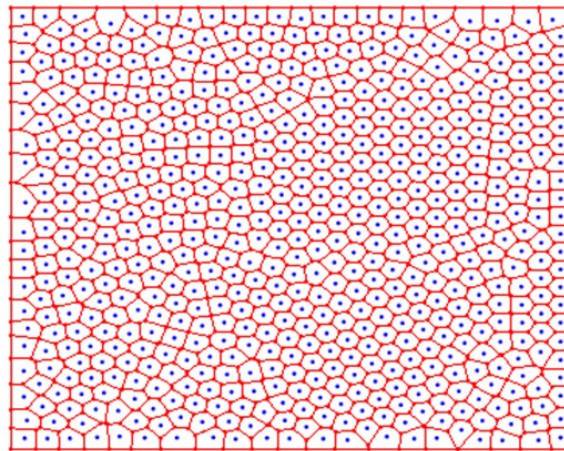
Figure 11: 2D irregular pore network model of wheat

3 Simulation and experimental study of wheat drying

Based on the 2D irregular pore network model of wheat, the heat and mass transfer process

during wheat drying is explored by simulation and experiments. A multiscale mathematical model is established to describe the wheat drying process, which is shown in Eqs. (7), (8), (10) and (11). A drying experiment is carried out to verify the simulation results.

3.1 Multiscale drying model based on the pore network model

Assumptions:

(1) Container scale

a) Heat transfer is dominated by convection, conduction and radiation are ignored.

b) Mass transfer is dominated by convection, diffusion and micro-scale effects are ignored.

c) Airflow and vapor are represented as incompressible ideal gas.

d) Heat and mass transfer are insulated by the container wall.

(2) Particle scale

a) No grain particle shrinkage and deformation during drying.

b) Uniform temperature distribution in grain particle during drying.

c) Moisture distribution in a grain particle depends on liquid or vapor diffusion.
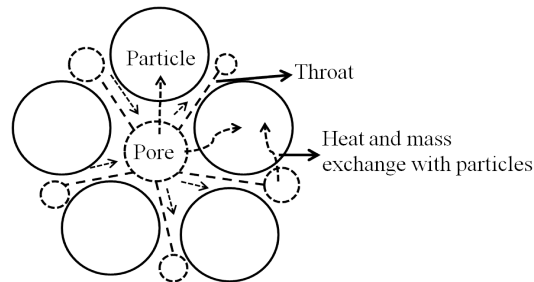
3.1.1 Momentum transfer equation

Darcy's law is used to describe the airflow passing through grain pile.

$$\varepsilon \frac{\partial \rho}{\partial t} = \nabla \cdot \left[\frac{\rho k^{*}}{\mu} \cdot \nabla \vec{P} \right] \tag{6}$$

The momentum equation can be obtained by discretizing the above equation:

$$\sum_{i_1=1}^{num_{i_1}} \pi \cdot r_t^2 \cdot \frac{k^{*n}}{\mu} \cdot \frac{P_i^n - P_{i_1}^n}{l_{t i_1}} = 0 \tag{7}$$

3.1.2 Heat and mass transfer equation on the container scale

Figure 12: The diagram of heat and mass transfer on the container scale

Based on the control volume method, the equilibrium relationship for each control volume can be obtained.

$$
\begin{cases}
V_{di} \cdot \dfrac{\rho_{vi}{}^{n} - \rho_{vi}{}^{n-1}}{\Delta t} = \sum_{e=1}^{num_e} (\pi r_{te}{}^{2} \cdot v_{te}{}^{n}) \cdot \rho_{ve}{}^{n} \\[2ex]
-\sum_{o=1}^{num_o} (\pi r_{to}{}^{2} \cdot v_{to}{}^{n}) \cdot \rho_{vi}{}^{n} + \sum_{i_3=1}^{num_{i_3}} \dfrac{A_g}{k_1} \cdot k_{i_3}{}^{n-1} \cdot \left(\rho_{veq,i_3}{}^{n-1} - \rho_{vi}{}^{n-1} \right) \\[2ex]
V_{di} \cdot \dfrac{\rho_i{}^{n-1} \cdot C_i{}^{n-1} \cdot T_i{}^{n} - \rho_i{}^{n-1} \cdot C_i{}^{n-1} \cdot T_i{}^{n-1}}{\Delta t} = \sum_{e=1}^{num_e} (\pi r_{te}{}^{2} \cdot v_{te}{}^{n}) \cdot \rho_e{}^{n-1} \cdot C_e{}^{n-1} \cdot T_e{}^{n} \\[2ex]
-\sum_{o=1}^{num_o} (\pi r_{to}{}^{2} \cdot v_{to}{}^{n}) \cdot \rho_i{}^{n-1} \cdot C_i{}^{n-1} \cdot T_i{}^{n} - \sum_{i_3=1}^{num_{i_3}} \dfrac{A_g}{k_1} h_{i_3}{}^{n-1} \left(T_i{}^{n-1} - T_{g,i_3}{}^{n-1} \right)
\end{cases}
\tag{8}
$$

3.1.3 Heat and mass transfer equation on particle scale

Since the evaporation rate from the grain surface is greater than the moisture diffusion rate in the grain, the grain drying rate decreases, and the grain temperature increases until it reaches the air temperature surrounding the grain. Luikov proposed the following equations to describe the slow drying process [Cao and Zhu (2001)].

$$
\begin{cases}
\dfrac{\partial M}{\partial t} = \nabla^2 G_{11} M + \nabla^2 G_{12} T + \nabla^2 G_{13} P \\[2ex]
\dfrac{\partial T}{\partial t} = \nabla^2 G_{21} M + \nabla^2 G_{22} T + \nabla^2 G_{23} P \\[2ex]
\dfrac{\partial P}{\partial t} = \nabla^2 G_{31} M + \nabla^2 G_{32} T + \nabla^2 G_{33} P
\end{cases}
\tag{9}
$$

The value of G is related to temperature, moisture and pressure.

To simplify the calculation, the grain particle is taken as continuous media, as shown in Fig. 13.
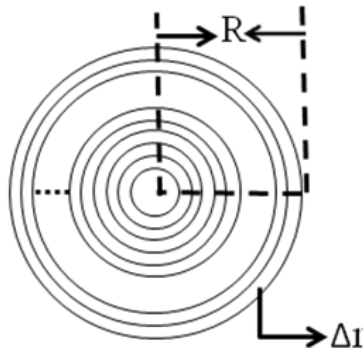
Figure 13: Schematic diagram of particle discretization

Combined the heat conservation formula, the discrete heat and mass transfer equation on the particle scale is as follows.

$$
\begin{cases}
M_m^{j+1} = K_1(1-\dfrac{1}{m})M_{m-1}^j + (1-2K_1)M_m^j + K_1(1+\dfrac{1}{m})M_{m+1}^j \\[2mm]
M_m^1 = M_0(r_m),\ m = 1,2,\ldots,m_t \\[2mm]
M_m^{j+1} = M_m^j + 6K_1(M_2^j - M_1^j) \\[2mm]
M_{m_t}^{j+1} = (1 - k_1 k_2 - 3k_2 + k_3 k_4)M_{m_t}^j + k_2 M_{m_t-1}^j + k_4 M_e \\[2mm]
k_1 = \dfrac{3\Delta r}{R},\ k_2 = \dfrac{D\Delta\tau}{3\Delta r^2/4},\ k_3 = \dfrac{2D}{\Delta rk},\ k_4 = \dfrac{(k_1+2)k_2}{1+k_3} \\[2mm]
Q_1^{\,n-1} = W^{n-1} \cdot h_{fg}^{\,n-1} \\[2mm]
Q_2^{\,n-1} = \displaystyle\sum_{i=1}^{k_1} \dfrac{W^{n-1}}{k_1} \cdot C_v^{\,n-1} \cdot \left(T_i^{\,n-1} - T_g^{\,n-1}\right) \\[3mm]
Q_3^{\,n-1} = \left(\rho_g \cdot C_g + \rho_g \cdot M^{n-1} \cdot C_w^{\,n-1}\right) \cdot V \cdot \dfrac{T_g^{\,n-1} - T_g^{\,n-2}}{\Delta t} \\[3mm]
Q^{n-1} = \displaystyle\sum_{i=1}^{k_1} h^{n-1} \cdot \dfrac{A_g}{k_1} \cdot \left(T_i^{\,n-1} - T_g^{\,n-1}\right) \\[3mm]
Q^{n-1} = Q_1^{\,n-1} + Q_2^{\,n-1} + Q_3^{\,n-1} \\[2mm]
\dfrac{dT_g}{dt} = \dfrac{Q - Q_1 - Q_2}{(\rho_g \cdot C_g + \rho_g \cdot M \cdot C_w) \cdot V}
\end{cases}
\tag{10}
$$

3.1.4 Heat and mass exchange equation between two scales

Fig. 14 shows the heat and mass exchange between the two scales; and the heat and mass exchange control equation can be obtained.
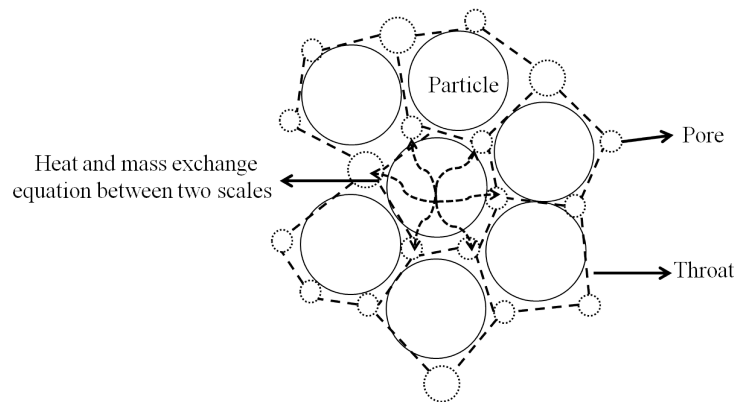
Figure 14: The diagram of heat and mass transfer between the container scale and particle scale

$$
\begin{cases}
\sum_{i_3=1}^{num_{i_3}} \dfrac{\rho_g \cdot \dfrac{4}{3}\pi R^3 \cdot \dfrac{\sum\limits_{m=1}^{m_t} M\left(m\cdot\Delta r,(n-1)\Delta t\right) - \sum\limits_{m=1}^{m_t} M\left(m\cdot\Delta r,(n-2)\Delta t\right)}{m}}{k_1} \\[4ex]
= \sum_{i_3=1}^{num_{i_3}} \dfrac{A_g}{k_1} k_{k_1}{}^{n-1}\left(\rho_{veq,k_1}{}^{n-1} - \rho_{vi}{}^{n-1}\right) \\[3ex]
\sum_{i=1}^{i_3} h^n \cdot \dfrac{A_g}{k_1}\cdot\left(T_i{}^n - T_g{}^n\right) = \\[3ex]
\sum_{i_3=1}^{num_{i_3}} \dfrac{W^n \cdot h_{fg}{}^n + \sum\limits_{i=1}^{k_1}\dfrac{W^n}{k_1}\cdot C_v{}^n\cdot\left(T_i{}^n - T_g{}^n\right) + \left(\rho_g\cdot C_g + \rho_g\cdot M^n\cdot C_w{}^n\right)\cdot V\cdot\dfrac{T_g{}^n - T_g{}^{n-1}}{\Delta t}}{k_1}
\end{cases}
\tag{11}
$$

These equations can be simplified into series of linear equations and solved by MATLAB software.

3.2 Wheat drying experiment

3.2.1 Materials, instruments and equipment

Material: The initial moisture content of wheat is too low to be dried. Therefore, the initial moisture content should be raised by humidification. Wheat is immersed into water for 24 hours, spread on the floor into a 2-cm thickness and turned frequently until its dry-basis moisture content is approximately 25%, and then piled to make it uniform.

Instruments: Electronic balance (FB224, Shunyuhengping, China), hand-held temperature and humidity meter (HMP76, Vaisala, Finland), and infrared thermal imager (Testo 875-1i, Testo, Germany).

Equipment: Oven (DHG-9140A, Jinghong, China), and small bin with the length, width and height of 0.6 m×0.6 m×1.2 m as shown in Fig. 15.

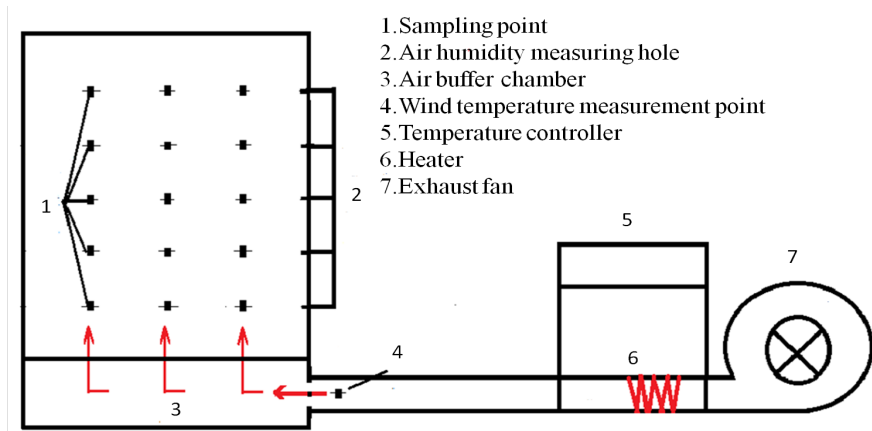1. Sampling point
2. Air humidity measuring hole
3. Air buffer chamber
4. Wind temperature measurement point
5. Temperature controller
6. Heater
7. Exhaust fan

Figure 15: Schematic structure of the small bin

3.2.2 Operating conditions and methods

Drying experiments were carried out in the bin (Fig. 15) under the operation conditions shown in Tab. 2. A U-shape orifice plate was used to simulate the U-shape ventilation duct structure in real bins. The grain temperature and moisture content at different sampling positions and time intervals were measured quickly to minimize the effect of environmental conditions. The sampling device and 4 sampling positions at the same grain layer are shown in Fig. 16. The holes in the sampler determine the sampling positions in the depth direction.

**Table 2:** Operating conditions of drying experiments

| Parameter	Unit	Value
Ambient temperature	°C	20.66
Absolute humidity of environment	g/m³	1.69
Initial wheat temperature	°C	20.66
Initial moisture content of wheat	%	23.53
Air temperature at inlet	°C	62
Bed thickness	m	0.65
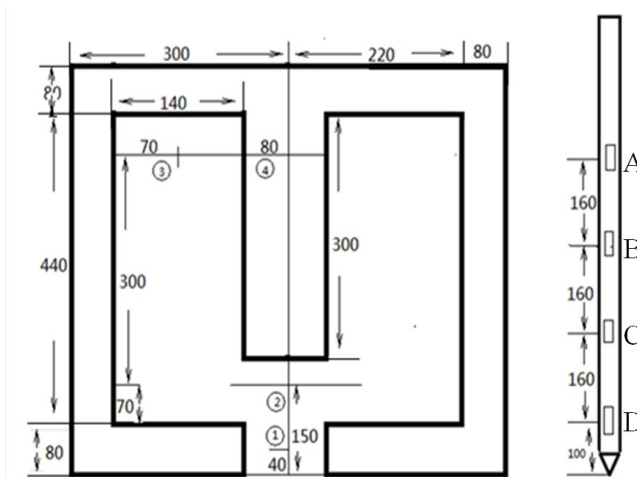
Figure 16: U-shape orifice plate, sampling positions and sampler

3.2.3 Experimental results and analysis

Limited by the computational workload, only the material with a layer thickness of 10 cm close to the orifice is selected as the simulation area in this study. Fig. 17 shows the moisture content of wheat at different drying times and sampling positions at layer D. The moisture content of wheat at the same layer is almost same, and the unevenness of the moisture content is less than 2.5%. Comparing the drying curves at 4 sampling points, the drying rate at point 2 is larger than that at point 1. It means that the drying rate at the inlet boundary is less than that at the inlet corner.
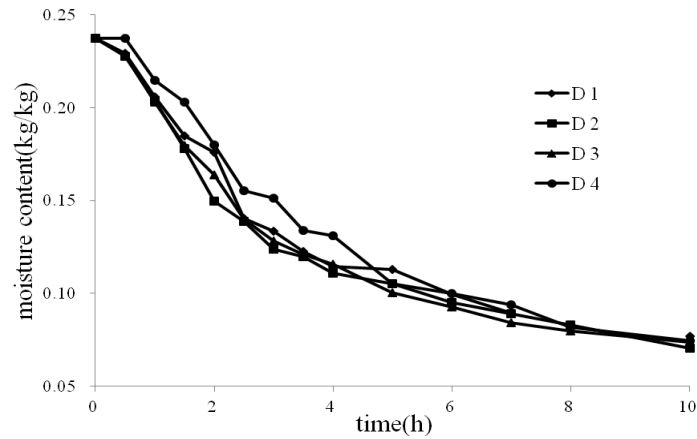
Figure 17: Moisture content of wheat kernel at layer D
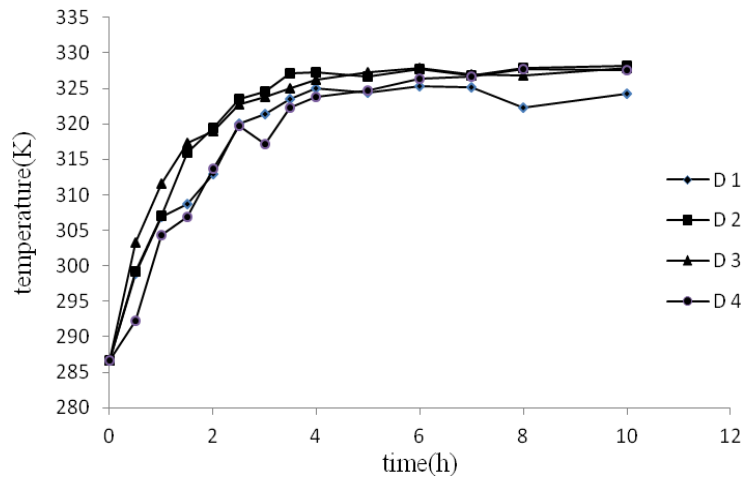
Figure 18: Wheat temperatures at layer D

The wheat temperatures at layer D are almost consistent and change with drying time, as shown in Fig. 18. The wheat temperature rises rapidly at first, and then slowly becomes close to the ambient air temperature. The wheat temperature at point 2 is obviously higher than that at point 4.

3.3 Simulation of wheat drying process

3.3.1 Initial conditions and boundary conditions

The initial dry-basis moisture content of wheat was 0.2353; the initial wheat temperature was 293.81 K; the inlet air pressure was 52.18 Pa, the vapor density was 0.00169 kg/m^3; the inlet air temperature was 335.15 K; and the initial internal air temperature was 293.81 K. The center coordinates of the sampled pores and particles are listed in Tab. 3.

**Table 3:** Coordinates of the sampled pores and particles

| Sample pore	x/m	y/m	Sample particle	x/m	y/m
1	0.0041	0.0033	1	0.0027	0.0023
2	0.0951	0.0024	2	0.0881	0.0029
3	0.0590	0.0477	3	0.0541	0.0507
4	0.0026	0.0921	4	0.0075	0.0961
5	0.0851	0.0913	5	0.0890	0.0973

3.3.2 Analysis of the simulation results

Fig. 19 compares the simulated average moisture content with the experimental results. The simulated moisture content decreased from 0.2353 to 0.0710 in approximately 9.3 hours, which is slightly faster than the experiment. In the early drying stage, the simulated drying rate is similar to the experimental drying rate. However, the simulated drying rate slows down as it approaches a later stage. When the final moisture content is the same, the drying time required for the experiment and simulation is almost the same. The experimental drying rate that is faster than the simulated results may be caused by the sampling process, which will disturb the stable state and form an airflow channel with a larger porosity than other areas in the grain pile.

Fig. 20 depicts the vapor densities in different sampling points in the three-layer depth. The closer to the bottom, the larger the vapor density is. This is because the vapor at the top layer is easily removed from the thin grain pile by hot air. All vapor densities in different sampling points initially increase with the moisture being removed easily and quickly from the wheat at the beginning stage, but gradually decrease when the moisture content decreases and the water inside the wheat becomes increasingly more difficult to be removed at the later drying stage.
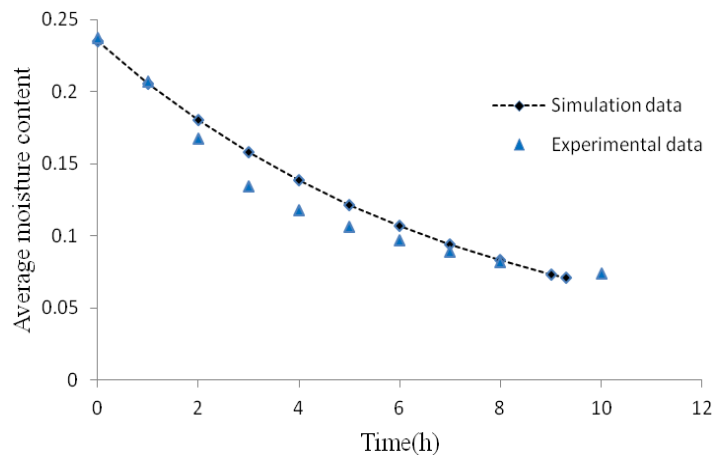
Figure 19: Drying curve of wheat
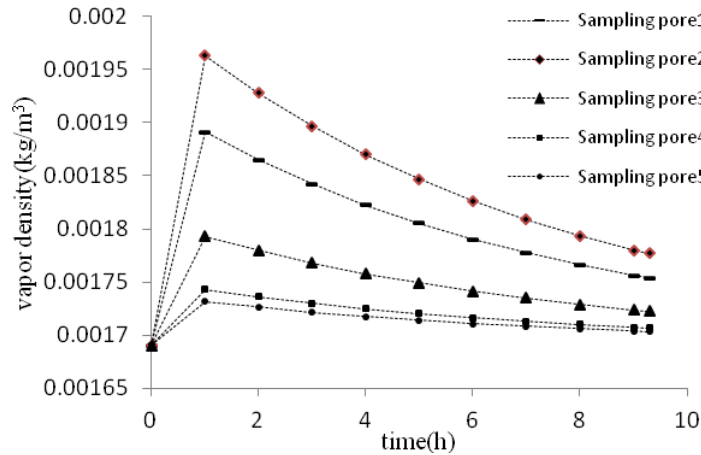
Figure 20: Vapor densities in sampling pores
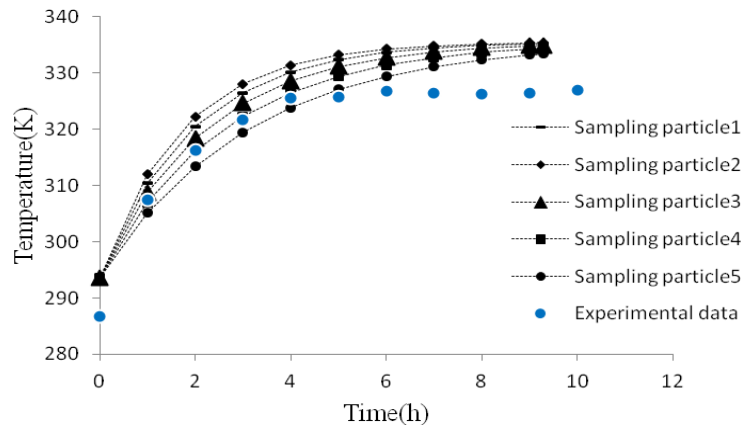
Figure 21: Wheat temperatures at the sampling position

Fig. 21 shows the simulated wheat temperature at different positions. The closer to the bottom, the higher the wheat temperature is, which occurs because wheat at the low layer is heated by the hottest air. The average simulated wheat temperature is higher than the average wheat temperature measured at 4 sampling points, as shown in Fig. 16. The measured low wheat temperature might be caused by the instrument test accuracy (±2°C), measurement error (wheat temperature decreases quickly under room temperature in winter), and the initial temperature error between the actual wheat temperature and the assigned value. The wheat temperature gradually increases to the inlet air temperature.

The air temperatures in the sampling pores can be observed in Fig. 22. As a large amount of heat required for vaporization is absorbed from air, the air temperature decreases at the beginning drying stage, and then increases and approaches the inlet air temperature with less moisture evaporation.
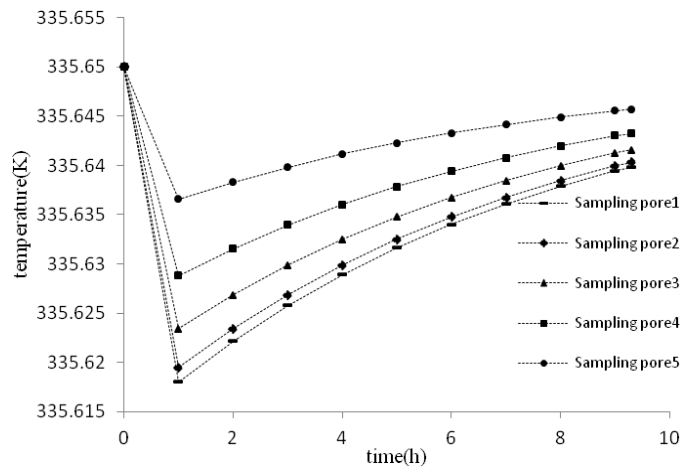
Figure 22: Air temperatures in sampling pores

4 Conclusions

1) A 2D irregular pore network model was constructed based on the image of monolayer material, and the distribution of extracted particle sizes is similar to that of the real particles.

2) The pore space parameters of the reconstructed irregular pore network model are similar to the extracted parameters from a 2D image. The reconstruction method can be used for reconstruction of an irregular pore network model with a random size.

3) The established multiscale heat and mass transfer model can simulate the drying process of wheat and be verified by experiments. It proves that the pore network model can effectively describe the actual pore structure of stacking unconsolidated material.

References

Abbouda, S. K.; Al-Amri, A. M. S. (2001): Application of heat transfer model for prediction of temperature distribution in stored wheat. *Agricultural Mechanization in Asia, Africa and Latin America*, vol. 32, no. 3, pp. 46-50.

Al-Amri, A. M.; Abbouda, S. K. (2004): Application of a mass transfer model for simulation and prediction of moisture distribution in stored corn grains. *Scientific Journal of King Faisal University (Basic and Applied Sciences)*, vol. 5, pp. 197-213.

Banerjee, R.; Bevilacqua, N.; Eifert. L.; Zeis. R. (2019): Characterization of carbon felt electrodes for vanadium redox flow batteries-A pore network modeling approach. *Journal of Energy Storage*, vol. 21, pp. 163-171.

Cao, C. W.; Zhu, W. X. (2001): *Computer Simulation of Drying Process of Agricultural Products*. Beijing: China Agriculture Press.

Daian, J. F.; Saliba, J. (1991): Determining a representative random pore-network for moisture sorption and migration in cement mortar. *International Journal of Heat and Mass Transfe*r, vol. 34, pp. 2081-2096.

Erickson, D.; Li, D.; Park, C. B. (2002): Numerical simulations of capillary-driven flows in nonuniform cross-sectional capillaries. *Journal of Colloid & Interface Science*, vol. 250, pp. 422-429.

Fatt, I. (1956): The network model of porous media. *Society of Petroleum Engineers*, vol. 207, pp. 144-181.

Gharedaghloo, B; Price, J. S; Rezanezhad, F; Quinton, W. L. (2018): Evaluating the hydraulic and transport properties of peat soil using pore network modeling and X-ray micro computed tomography. *Journal of Hydrology*, vol. 561, pp. 494-508.

Gong, Y. Z.; Niu, H. X.; Dong, Z. M.; Liu, X. D. (2009): Construction of pore network model of fractal porous media. *Journal of Agricultural Machinery*, vol. 1, pp. 108-114.

Hammami, F.; Ben, Mabrouk. S.; Mami, A. (2016): Modelling and simulation of heat exchange and moisture content in a cereal storage silo. *Mathematical and Computer Modelling of Dynamical Systems*, vol. 22, no. 3, pp. 207-220.

Jia, C. C.; Sun, D. W.; Cao, C. W. (2001): Computer simulation of temperature changes in a wheat storage bin. *Journal of Stored Products Research*, vol. 37, pp. 165-177.

Kharaghani, A.; Metzger, T.; Tsotsas, E. (2012): An irregular pore network model for convective drying and resulting damage of particle aggregates. *Chemical Engineering Science*, vol. 75, pp. 267-278.

Laurindo, J. B.; Prat, M. (1998): Numerical and experimental network study of evaporation in capillary porous media. Drying rates. *Chemical Engineering Science*, vol. 53, pp. 2257-2269.

Laurindo, J. B.; Prat, M. (1996): Numerical and experimental network study of evaporation in capillary porous media. Phase distributions. *Chemical Engineering Science*, vol. 51, pp. 5171-5185.

Lu, B.; Torquato, S. (1992): Lineal-path function for random heterogeneous materials. *Physical Review A*, vol. 45, pp. 922-929.

Liu, M. C.; Wu, J.; Gan, Y. X.; Hanaor, D. A. H.; Chen, C. Q. (2018): Tuning capillary penetration in porous media: combining geometrical and evaporation effects. *International Journal of Heat and Mass Transfer*, vol. 123, pp. 239-250.

Ma, J. S.; Sanchez, J. P.; Wu, K. J.; Couples, G. D.; Jiang, Z. Y. (2014): A pore network model for simulating non-ideal gas flow in micro- and nano-porous materials. *Fuel*, vol. 116, pp. 498-508.

Oren, P. E.; Bakke, S. (2002): Process based reconstruction of sandstones and prediction of transport properties. *Transport in Porous Media*, vol. 46, pp. 311-343.

Prat, M. (1993): Percolation model of drying under isothermal conditions in porous-media. *International Journal of Multiphase Flow*, vol. 19, pp. 691-704.

Prat, M. (1995): Isothermal drying on non-hygroscopic capillary-porous materials as an invasion percolation process. *International Journal of Multiphase Flow*, vol. 21, pp. 875-892.

Salama, A. (2018); Interface tracking of an oil ganglion inside a cascade of pore bodies and pore throats: a quasistatic investigation. *Chemical Engineering Science*, vol. 192, pp. 467-476.

Segura, L. A.; Toledo. P. G. (2005): Pore-level modeling of isothermal drying of pore networks accounting for evaporation, viscous flow, and shrinking. *Drying Technology*, vol. 23, pp. 2007-2019.

Wang, Y.; Kharaghani, A.; Metzger, T.; Tsotsas, E. (2012): Pore network drying model for particle aggregates: assessment by x-ray microtomography. *Drying Technology*, vol. 30, pp. 1800-1809.

Wang, Y.; Pu, J.; Wang, L. H.; Wang, J. Q.; Jiang, Z. et al. (2016): Characterization of typical 3d pore networks of jiulaodong formation shale using nano-transmission X-ray microscopy. *Fuel*, vol. 170, pp. 84-91.

Wang, J. Q.; Zhao, J. F.; Zhang, Y.; Wang, D. Y.; Li, Y. H. et al. (2016): Analysis of the effect of particle size on permeability in hydrate-bearing porous media using pore network models combined with CT. *Fuel*, vol. 163, pp. 34-40.

Xu-Dong, L. I. (2005): Internal and external common tangent circles of three circles which are externally tangent each other. *Journal of Youjiang Teachers College for Nationalities Guangxi*, vol. 18, pp. 6-8.

Xie, D.; Wang, Y.; Wang, H. Q.; Mo, S. Q.; Liao, M. L. (2016): Numerical analysis of temperature non-uniformity and cooling capacity for capillary ceiling radiant cooling panel. *Renewable Energy*, vol. 87, pp. 1154-1161.

Yang, B. (2006): *Fractal Pore Network Simulation and Experimental Research on Drying of Porous Media*. Beijing: China Agricultural University.

Young, W. B. (2004): Analysis of capillary flows in non-uniform crosssectional capillaries. *Colloids & Surfaces A Physicochemical& Engineering Aspects*, vol. 234, pp. 123-128.

Yu, P.; Duan, Y. H.; Chen, E.; Tang, S. W.; Wang, X. R. (2018): Microstructure-based fractal models for heat and mass transport properties of cement paste. *International Journal of Heat and Mass Transfer*, vol. 126, pp. 432-447.

Yuan, Y. J.; Tan, L. B.; Zhao, Z.; Xu, Y. Y.; Zhao, Y. et al. (2016): Multiscale and multilayer structural modeling and simulation on drying of grain packing porous media. *Drying Technolog*y, vol. 34, pp. 1664-1676.

Yue, R.; Zhang, Q. (2017). A pore-scale model for predicting resistance to airflow in bulk grain. *Biosystems Engineering*, vol. 155, pp. 142-151.

Yao, J.; Zhao, X. C.; Yi, Y. J. (2005): The status and prospect of digital core technology. *Petroleum Geology and Recovery Efficiency*, vol. 12, pp. 52-54.

Zhao, Y.; Liu. L.; Han, Q. L.; Zhao, Y. D. (2018): Reconstruction of soil pore structure based on CT images. *Journal of Agricultural Machinery*, vol. 49, pp. 401-406.